
MODELING BEAM PROPAGATION AND FREQUENCY CONVERSION FOR THE BEAMLET LASER

J. M. Auerbach

Introduction

The development of the Beamlet laser has involved extensive and detailed modeling of laser performance and beam propagation to: (1) predict the performance limits of the laser, (2) select system configurations with higher performance, (3) analyze experiments and provide guidance for subsequent laser shots, and (4) design optical components and establish component manufacturing specifications.

In contrast to modeling efforts of previous laser systems such as Nova,¹ those for Beamlet include as much measured optical characterization data as possible. This article concentrates on modeling of beam propagation in the Beamlet laser system, including the frequency converter, and compares modeling predictions with experimental results for several Beamlet shots. It briefly describes the workstation-based propagation and frequency conversion codes used to accomplish modeling of the Beamlet.

Propagation Modeling

PROP92 is the new family of single-wavelength propagation codes. It includes PROP1, a code for one-dimensional geometries; PROP2, a code for two-dimensional geometries; and HANK (derived from the HANKEL transforms), a code for circularly symmetric geometries. Multi-wavelength processes, such as frequency conversion, are modeled using other codes. Phase retardation, due to the nonlinear index of refraction, is the only nonlinear process modeled in the PROP92 set of codes. The linear processes that are modeled include bulk and reflective losses and the refractive index effects on propagation length. Amplifier gain is modeled by treating laser slabs as Frantz-Nodvick saturable amplifiers. The codes can thus model spatially varying gain, depletion of gain due to energy extraction, and saturation effects at high extraction.

The “chain editor” is a powerful feature of the PROP92 codes, which allows a complex laser system to be described using a compact, simple input format. By using simple path definitions, the laser beam can be propagated in a multitude of different paths. This is especially useful for Beamlet, which consists of a multipass amplifier cavity that uses a Pockels cell and polarizer to switch the beam out of the cavity.

A useful feature of the PROP1 and PROP2 codes is their capability to assign measured spatial distributions of gain, transmission, or phase to each optical component, which is crucial to accurate modeling of laser systems. Spatial gain distribution measurements of the interior and end slabs of the Beamlet amplifier are discussed in detail in “Design and Performance of the Beamlet Amplifiers,” p. 18. (Specifically, Fig. 4 of that article illustrates the diamond, interior, and X slab configuration.) This data is stored in three files—one corresponding to the interior slab and one for each end slab configuration. In a PROP1 or PROP2 input file, each file is assigned to the corresponding amplifier slab defined in the system configuration file.

The phase aberration data consists of two main parts: (1) dynamic or “pump induced” aberrations that are a result of thermally induced distortions produced by flash-lamp pumping of the laser slabs, and (2) static distortions that arise from optical inhomogeneities in the bulk optical material or surface imperfections caused by the finishing process. Beam-steering measurements have been performed to determine the pump-induced aberrations in each amplifier slab configuration as discussed in “Design and Performance of the Beamlet Amplifiers,” p. 18. The static aberrations of amplifier slabs, potassium dihydrogen phosphate optical switch and converter crystals, and other optical components have been measured using phase shift interferometry. The phase map data are stored in files and can be

arbitrarily assigned as an aberration to an optical component. These phase maps range in size from $40\text{ cm} \times 40\text{ cm}$ to $3\text{ cm} \times 3\text{ cm}$. The larger maps contain phase data with ripple scale lengths resolved to a few millimeters. The smaller phase maps contain phase data with ripple scale lengths resolved to less than a millimeter.

Transmission masks can also be used by the codes to simulate the effects of various apertures in the propagation path. The most important application for a transmission mask is to model a beam apodizer. For example, the input apodizer for Beamlet is a serrated aperture. The Beamlet input list references a file that holds a transmission mask for a serrated aperture.² This mask file was created using a code specifically designed to create serrated aperture transmission patterns.

The PROP1, PROP2, and HANK codes are also capable of including spatial filter/optical relay information. The spatial filter is the optical component used to reduce or eliminate optical component noise. It consists of a set of confocal lenses and a pinhole. The pinhole can be circular or rectangular in shape. The parameters for defining the filter in the model are the focal length of the input lens, the magnification, and the size and shape of the pinhole.

In Beamlet's front end, there is an additional beam-shaping component, called a gain compensator mask, that compensates for the amplifier slab gain roll-off due to amplified spontaneous emission. In the following examples, the gain compensator produces a spatially flat intensity distribution in the output beam. Figure 1(a) shows a calculated beam profile after it has passed through a compensator mask transmission profile, which is parabolic in the x -direction and uniform in the y -direction. The minimum transmission of the mask is 0.3 and the spatial separation between the 0.3 transmission point and the near unity peak transmission is 1.5 mm. Figure 1(b) shows the measured profile of a continuous-wave laser beam after it has passed through one of the actual masks used in Beamlet.

To illustrate the capability of the PROP92 codes, we modeled the $1.053\text{-}\mu\text{m}$ propagation through Beamlet using PROP2. The simulation corresponds to an actual experiment in which Beamlet produced 6.6 kJ of energy at $1.053\text{ }\mu\text{m}$ in a temporally flat pulse of 3 ns duration. Figure 2 shows a schematic of the laser system. The simulation starts at the serrated apodizer and ends at the input to the frequency converter. An output fluence of $\sim 9\text{ J/cm}^2$ is specified for a temporally flat pulse shape. PROP2 automatically calculates the input fluence and the temporal shape of the input pulse required for these output conditions.

In the PROP2 simulation of Beamlet, the following "real" optical component characteristics were used:

- Small signal gain profiles for the amplifier slabs,
- Pump-induced aberrations for the amplifier slabs,
- Static, large-scale ($L > 1\text{ cm}$) aberrations for the amplifier slabs, and
- Static aberrations ($L > 2\text{ mm}$) for the optical switch.

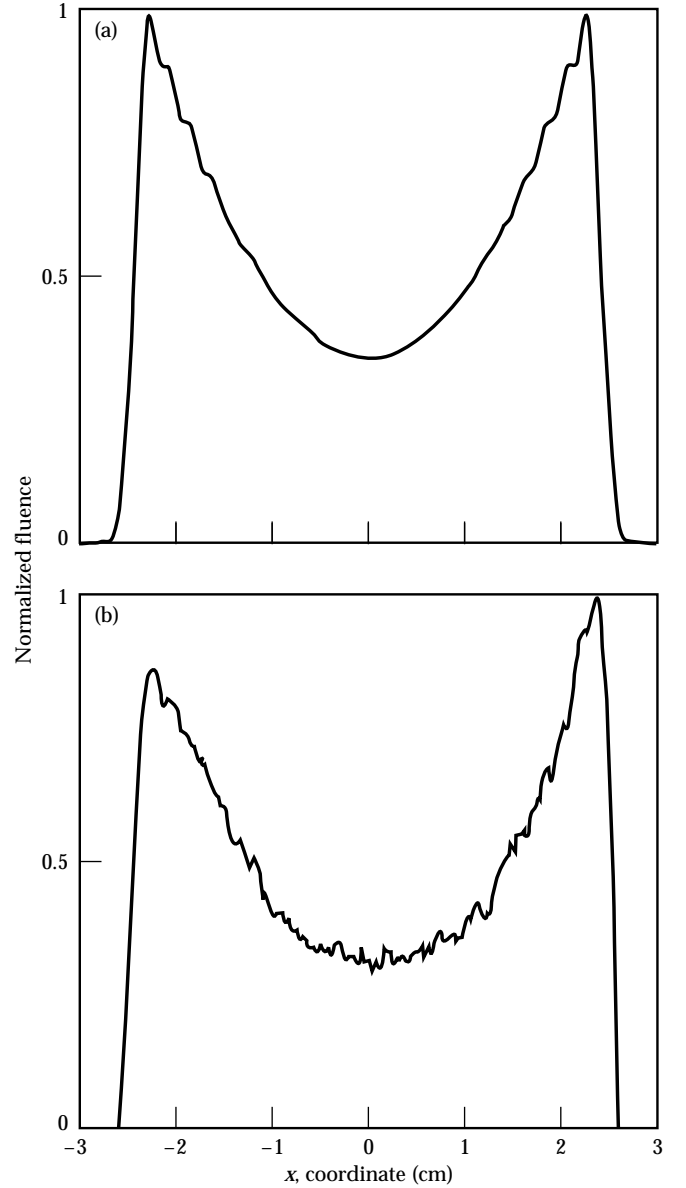


FIGURE 1. Comparison of (a) the modeled and (b) the measured transmission profiles of a continuous-wave laser beam through the gain compensation mask in the front end of Beamlet. (70-35-0195-0319pb01)

In the actual Beamlet, the amplifier slabs also have minor small-scale phase aberrations ($\sim\lambda/100$ peak-to-valley) that cannot be included in the modeling because of grid size limitations. Hence, we expect to see *less* small-scale modulation on calculated beam distributions as compared with actual beam distributions. In addition, PROP2 does not account for small obscurations that result from dust, scratches, or other minor imperfections in, or on, the optical components. These imperfections can lead to spikes in the fluence distribution.

Figure 3(a) shows the PROP2 calculated 1ω fluence central spatial x -profile at the laser system output, which is at the input plane of the frequency converter. The modulation at the top of the profile consists of both small- and large-scale phase aberrations. The small-scale modulation is due to the small-scale aberrations associated with the optical switch. The large-scale modulation is associated with pump-induced aberrations and large-scale static aberrations assigned to the amplifier slabs. Figure 3(b) shows the corresponding measured near-field fluence profile. Note that the measured small-scale modulation is larger than predicted with the model (not all the small-scale noise sources are included in the model). Large-scale modulation for both

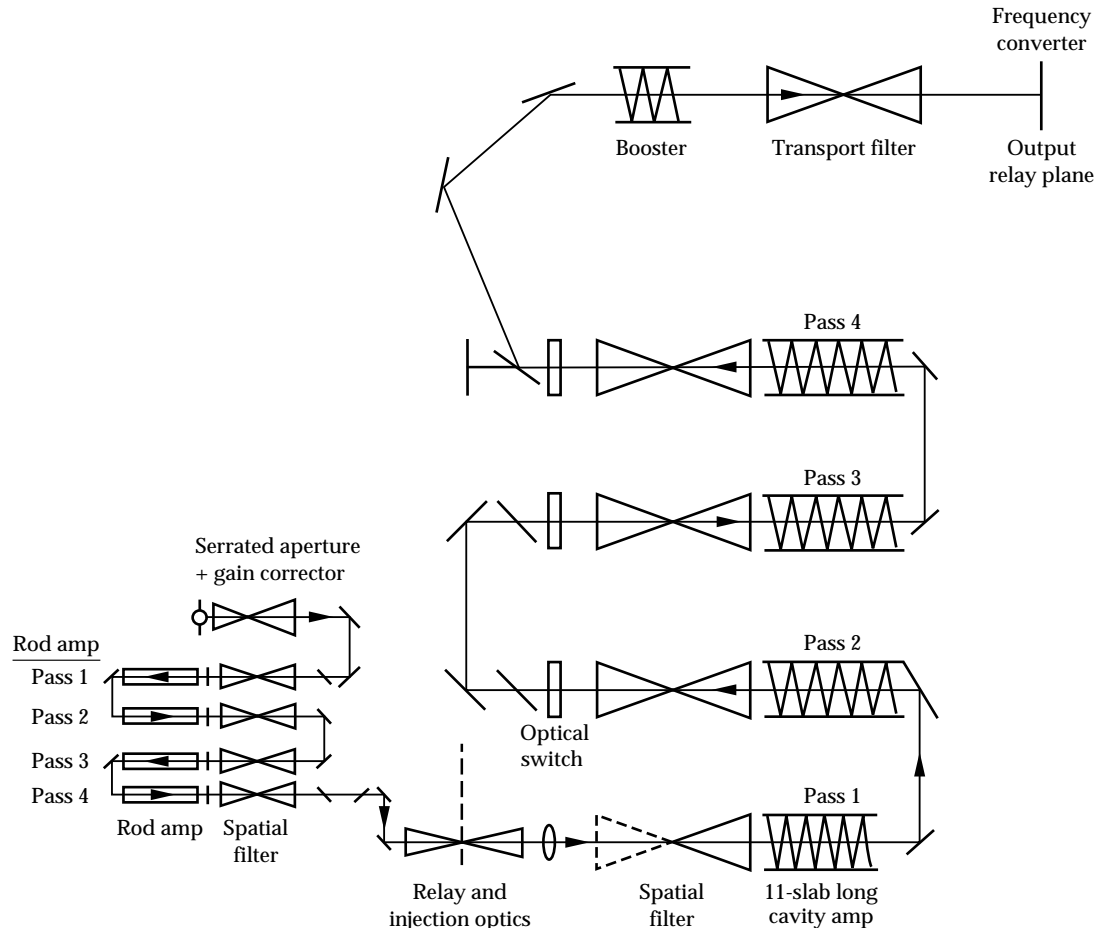
the measured and calculated profiles are comparable.

To further illustrate Beamlet's modeling performance, we present the calculated and measured output fluence distributions of a Beamlet high-energy shot. In this case, the output pulse has an energy of approximately 12 kJ and a 3.0-ns flat temporal shape. Figure 4 shows the calculated and measured central vertical profiles of fluence. The measured profile has more small-scale modulation than the model results since all small-scale phase noise sources could not be included in the calculation. Figure 5 shows the histogram based on calculated fluence data and the histogram based on measured fluence data at the input to the frequency converter. Note that the measured histogram has a higher peak abscissa value than the calculated histogram. We attribute the difference in the histograms to the fact that the phase noise source for the model does not contain all the noise sources that exist in Beamlet.

Frequency Conversion Modeling

To complement the PROP92 propagation codes, we have developed a family of codes to model frequency tripling in a dual-crystal scheme. The results have been

FIGURE 2. Schematic of the propagation path through the Beamlet laser system showing all the components from the serrated aperture in the front end to the frequency tripling system. This diagram shows optical components traversed by the beam during each pass. (70-35-0494-1900pb01)



in excellent agreement with the experiment. These codes have the following modeling capabilities for two-crystal conversion schemes:

- Frequency tripling of plane-wave, steady-state electric fields;
- Frequency tripling of plane-wave, time-varying electric fields—to model beams with applied bandwidth; and
- Frequency tripling of spatially varying (two transverse dimensions) steady-state electric fields—to model tripling of 1ω field distributions calculated by the PROP2 propagation code.

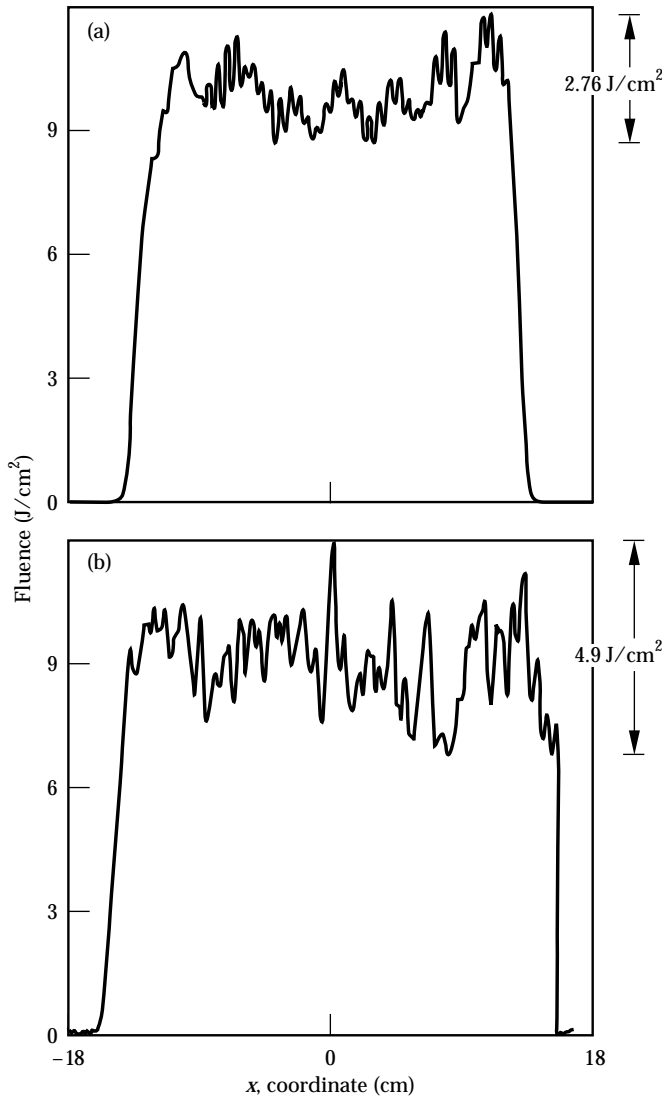


FIGURE 3. Comparison of (a) the modeled prediction and (b) the measured horizontal intensity profile at the input to the frequency converter. The predicted mean output fluence is approximately 9 J/cm^2 at a pulse width of 3.0 ns and energy of 6.8 kJ . This compares with the measured energy of 6.6 kJ at a pulse width of 3.0 ns . (70-35-0195-0320pb01)

The codes account for the following physical processes and parameters: (1) Three-wave mixing (frequency doubling and frequency tripling), (2) nonlinear index phase retardation (B-integral), (3) paraxial diffraction and walkoff (spatially varying fields), (4) dispersion (temporally varying fields), (5) crystal bulk losses and surface reflections, and (6) crystal surface roughness (spatially varying fields). Item 6 is extremely important in modeling of 3ω beam transport after the converters. Small-scale phase ripples on the 3ω beam convert into intensity ripples by diffraction and nonlinear processes in 3ω transport optics. These intensity ripples and the associated nonlinear growth can lead to optical damage or poor focusability of the beam, or both.

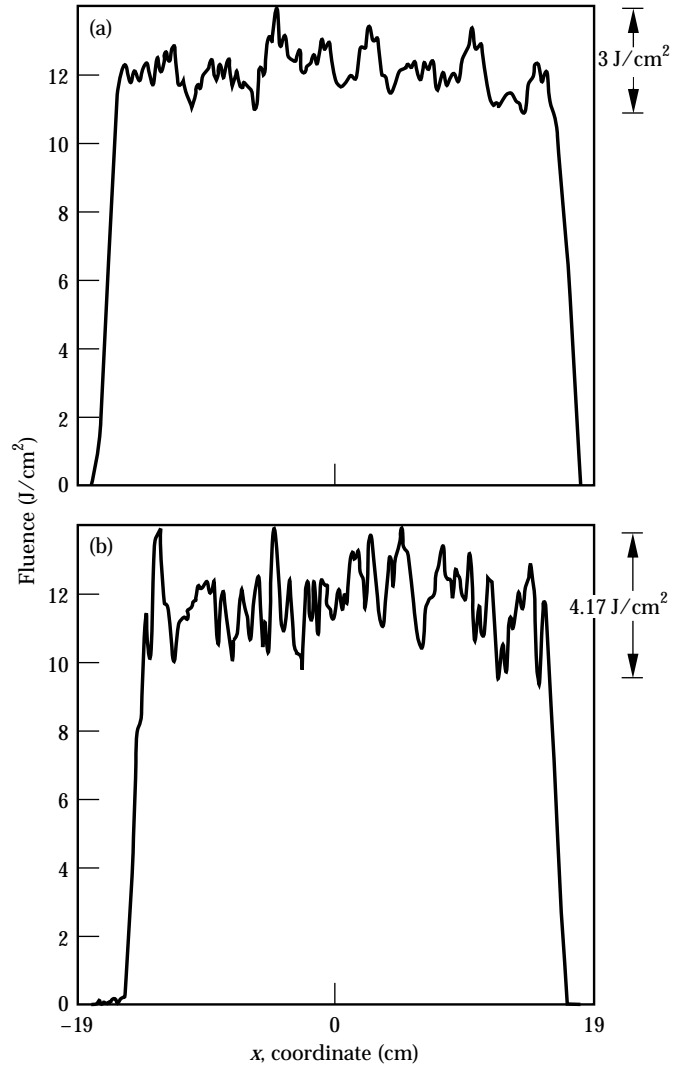


FIGURE 4. Comparison of (a) the modeled and (b) the measured horizontal intensity profile at the input to the frequency converter. The predicted mean output fluence is approximately 12 J/cm^2 . The output pulse is temporally flat with a width of 3.0 ns and an energy of 12.6 kJ . This compares with the measured pulse of 12.0 kJ at a pulse width of 3.0 ns . (70-35-0195-0318pb01)

The time-dependent plane-wave code was used to model Beamlet's 3ω output for a 1ω temporally flat input beam that is phase modulated at 30 GHz bandwidth and has a 1ω intensity range of 2–4 GW/cm². Figure 6 shows the calculated 3ω conversion efficiency as a function of 1ω intensity for the case of no-added bandwidth and 30-GHz bandwidth phase modulation. It also shows the measured 3ω conversion efficiency values. The departure at high intensities between calculated and measured values is attributed to spatial intensity and phase variations in the actual beam compared with the ideal plane wave assumed in the model. Also, at high intensities, conversion efficiencies are more

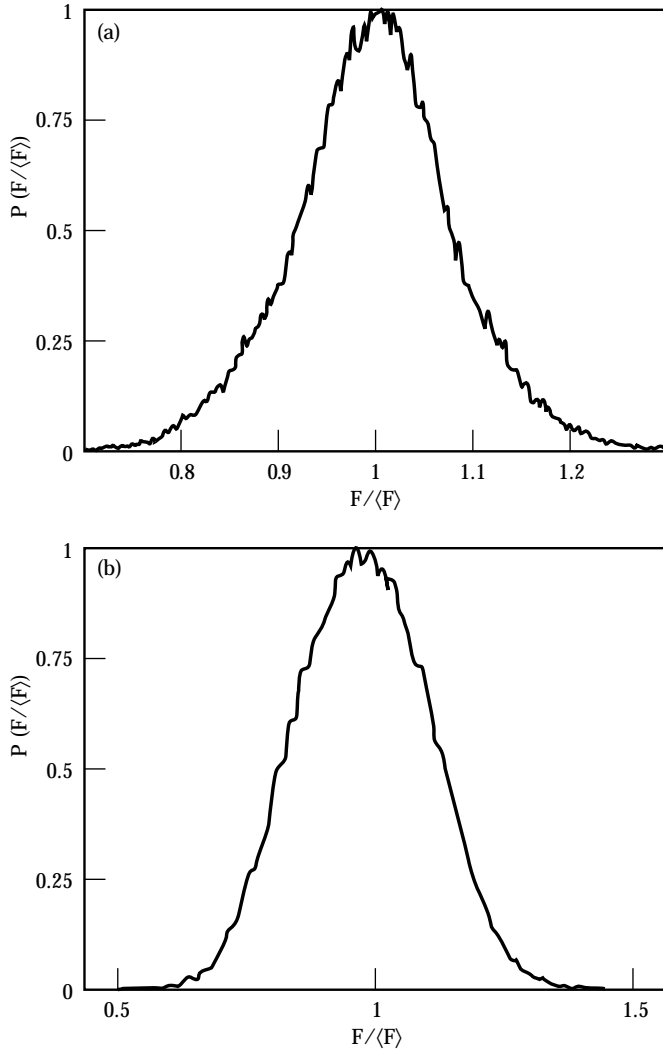


FIGURE 5. Comparison of (a) the modeled and (b) the measured fluence histograms for the Beamlet performance with a 3.0-ns temporally flat pulse with an energy of approximately 12 kJ. The histogram for the measured data has a higher peak abscissa value since the model does not include all noise sources. (70-35-0195-0321pb01)

sensitive to crystal detuning errors. In the model, we assume a fixed set of detuning angles designed to give the maximum conversion efficiency. However, experimentally the crystal detuning angle is varied to try to achieve an optimum mix-ratio and conversion efficiency. The precision with which the crystal detuning angles can be set experimentally is limited by the accuracy of the crystal mounts and the accuracy with which the exact phase matching angle of the crystal can be determined.

We have also used the frequency conversion code that allows transverse spatial variation in the electric field to model the near-field 3ω intensity profile at the output of the Beamlet tripler. Figure 7 shows these results compared with the actual measured output. In this case, the mean input drive intensity is approximately 3 GW/cm² in a 3-ns square pulse and the measured conversion efficiency is about 80%. On average, the two profiles have the same amount of modulation, but their shapes are different since the calculation of the model input 1ω beam does not include all the optical component phase and noise sources that exist in the actual Beamlet laser system.

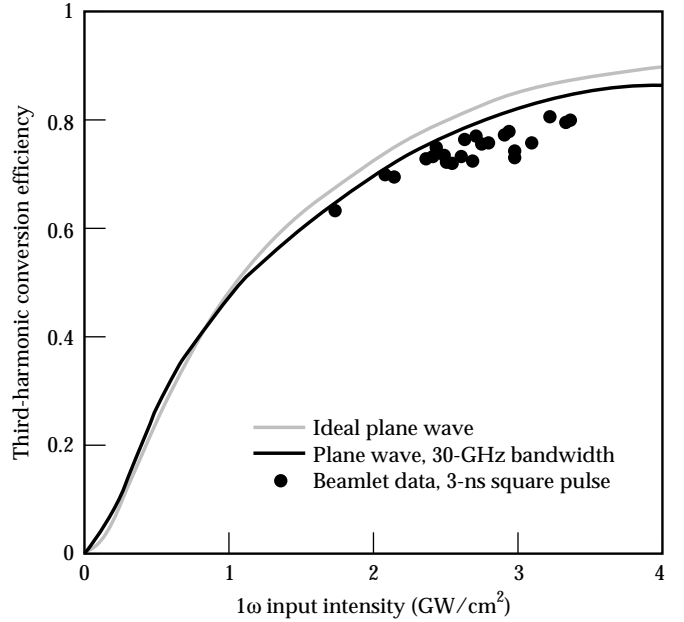


FIGURE 6. Calculated and measured values of 3ω conversion efficiency as a function of input 1ω intensity with 30 GHz of bandwidth applied to the 1ω input beam. (70-50-1094-3624pb02)

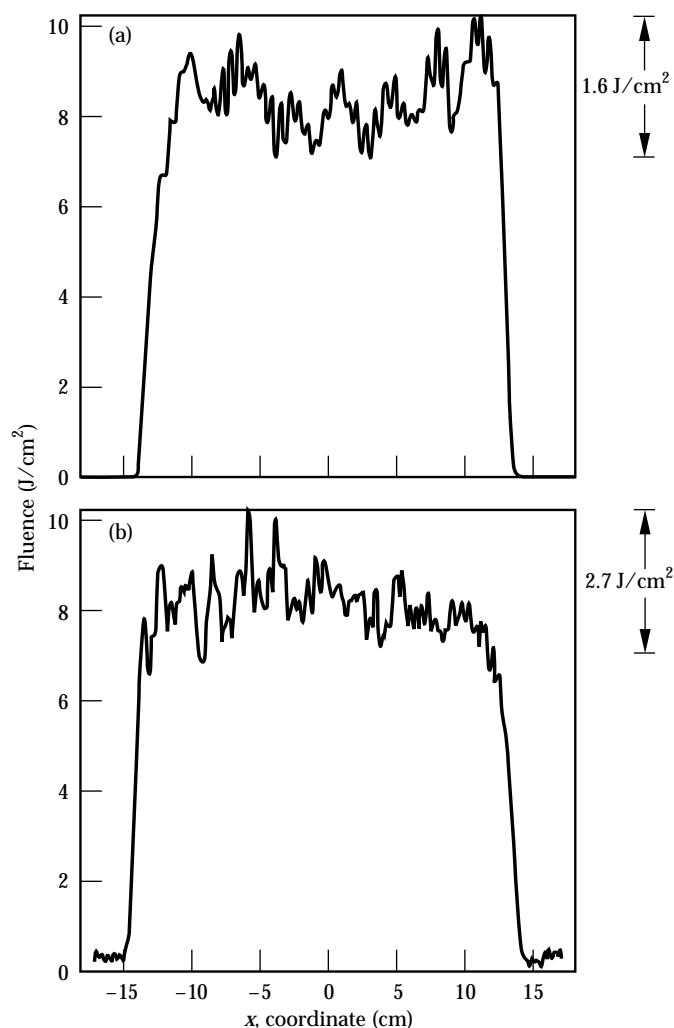


FIGURE 7. Comparison of (a) the modeled prediction and (b) the measured conversion efficiency for the 3ω fluence profiles at the output of the tripler crystal. (70-35-0195-0323pb01)

Summary

A new family of propagation and frequency conversion codes has been used to model Beamlet's performance. These codes incorporate many of the actual measured characteristics of the optical components. In general, the results of the model calculations are in good agreement with the measured Beamlet performance. The models have also proven to be a reliable tool for planning and guiding the experimental program.

Acknowledgments

The author acknowledges C. R. Wolfe, E. English, and M. Kellam for providing phase interferometry data on many of the Beamlet optics; R. Speck, B. Van Wouterghem, and other members of the Beamlet experimental team for their helpful technical discussions and for providing the experimental data that appear here; and J. Trenholme and J. Hunt for comments and input on certain aspects of this work.

Notes and References

1. W. W. Simmons, J. T. Hunt, and W. E. Warren, *IEEE Jour. Quant. Elect.*, QE-17 1727 (1981).
2. J. M. Auerbach and V. P. Karpenko, *Appl. Opt.* 33, 3179–3183 (1994).